Steady-State Parametric Optimization and Transient Characterization of Heat Flow Regulation With Binary Diffusion

Tanya Liu, James W. Palko, Joseph S. Katz, Feng Zhou, *Member, IEEE*, Ercan M. Dede, *Member, IEEE*, Mehdi Asheghi, *Member, IEEE*, and Kenneth E. Goodson, *Fellow, IEEE*

***Abstract*— Thermal regulators and switches are nonlinear devices that can greatly aid in the management of transient and/or spatially varying heating events. Various physical mechanisms have been harnessed to achieve nonlinear and switchable thermal behavior, though device characteristics are often evaluated in terms of steady-state performance only. Accurately capturing the transient behavior of these devices is a crucial missing link required for assessing the effectiveness of implementation in real-world scenarios. Here, we explore the physics of binary vapor diffusion through a noncondensable gas cavity as a promising mechanism for high-resistance contrast thermal regulation. Through a parametric steady-state optimization, we present a roadmap for future designs that can potentially reach switching ratios of up to 14.5. In addition, we perform a transient investigation to characterize the thermal response time of the device. The device possesses an extremely desirable attribute under certain transient heat loads, where the effective switching ratio appears significantly greater than the steady-state ratio due to a temporary increase in the OFF-state resistance immediately after switching. This work informs future experimental efforts for design optimization of binary-diffusion-based regulators and establishes simple modeling schemes to approximate device performance in system-level regulation scenarios.**

***Index Terms*— Regulators, temperature control, thermal management of electronics.**

Manuscript received April 24, 2020; revised June 19, 2020; accepted June 22, 2020. Date of publication June 30, 2020; date of current version December 23, 2020. This work was supported in part by the TOYOTA Research Institute of North America (TEMA) and in part by the National Science Foundation Engineering Research Center for Power Optimization of Electro Thermal Systems (POETS) under agreement EEC-1449548. The work of Tanya Liu was supported by the NSF Graduate Research Fellowship Program. The work of Joseph S. Katz was supported by Semiconductor Research Corporation (SRC) through the Graduate Research Fellowship. Recommended for publication by Associate Editor J. Punch upon evaluation of reviewers' comments. *(Corresponding author: Kenneth E. Goodson.)*

Tanya Liu, Mehdi Asheghi, and Kenneth E. Goodson are with the Department of Mechanical Engineering, Stanford University, Stanford, CA 94305 USA (e-mail: goodson@stanford.edu).

James W. Palko is with the Department of Mechanical Engineering, University of California at Merced, Merced, CA 95343 USA.

Joseph S. Katz was with the Department of Electrical Engineering, Stanford University, Stanford, CA 94305 USA. He is now with Exponent, Menlo Park, CA 94025 USA.

Feng Zhou and Ercan M. Dede are with the Toyota Research Institute of North America, Ann Arbor, MI 48105 USA.

This article has supplementary downloadable material available at https://ieeexplore.ieee.org, provided by the authors.

Color versions of one or more of the figures in this article are available online at https://ieeexplore.ieee.org.

Digital Object Identifier 10.1109/TCPMT.2020.3005880

I. Introduction

EFFECTIVE heat flow regulation is a ubiquitous requirement of multiple modern fields, including power electronics, energy storage and conversion, space, and biological functions [1]–[5]. A common goal of thermal regulation is to prevent significant spatial and/or temporal temperature deviations within a system, as many processes operate most effectively within a narrow temperature window. The electrical efficiency of photovoltaic systems for solar energy harvesting, for example, decreases by approximately 0.5% for each °C of temperature rise over ambient [6], [7]. Power converters used in ground/air transport are other prevalent application areas that benefit from strict temperature control, as thermal stresses generated from power cycling can lead to drastic reductions in lifetime reliability and performance degradation [8]. Conversely, thermal regulation may also be utilized to purposefully amplify the temperature difference within a system. Thermal energy harvesters, for example, demonstrate increased energy efficiency when operating with pulsed heating inputs [9]–[11]. When naturally occurring pulsed inputs are unavailable, appropriate thermal regulator usage can convert constant heat sources into oscillating heat sources [12]. Through all of the aforementioned applications, a critical opportunity emerges for the implementation of high-performance thermal devices that can dynamically respond to variations in environmental and operational thermal loads.

In contrast with conventional thermal management strategies typically represented as static resistances and capacitances, dynamic regulatory devices for enhanced thermal control exhibit nonlinear and switchable resistances. One method to control the thermal resistance between hot and cold surfaces is by improving/suppressing conduction heat transfer through making and breaking mechanical contact. Certain phenomena leveraged to achieve this mechanism include temperature or voltage-induced material flexing [13]–[16] and controllable liquid bridging [17]–[19]. Solid-state materials exhibiting a change in thermal resistance at a critical temperature can also act as passive thermal regulators [20]–[22]. The thermal conductance of crystalline polyethylene nanofibers, for instance, has been demonstrated to vary reversibly by up to 10x during structural phase transitions within a ∼10 °C temperature band [23]. Additional regulation schemes that can demonstrate highly variable thermal resistances include

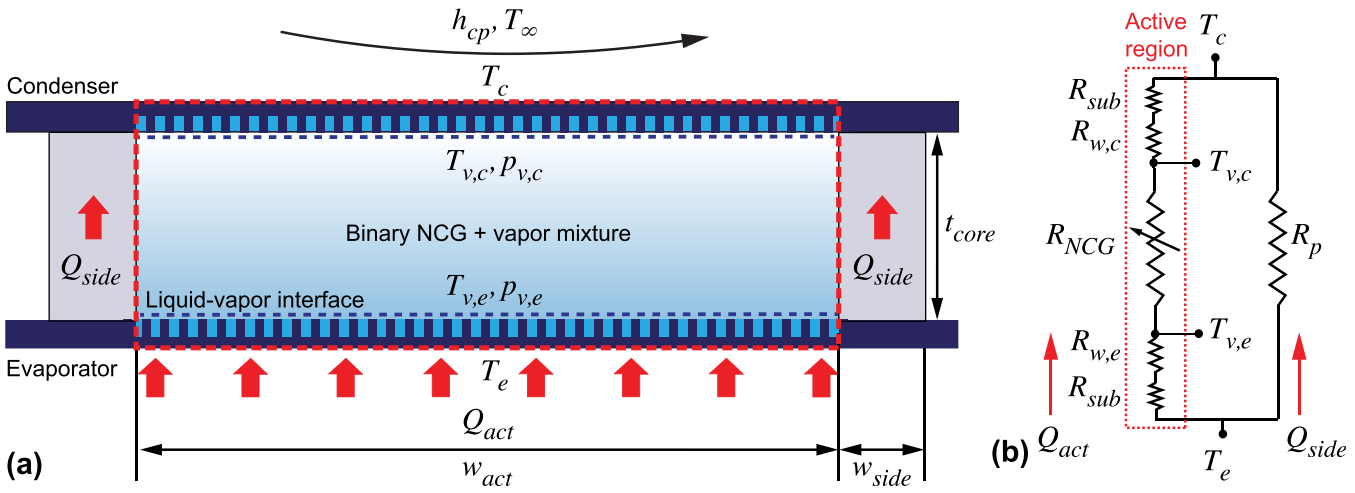

Fig. 1. (a) Thermal regulator cross-sectional schematic. The heated liquid evaporates from a porous wick, diffuses through an NCG-filled cavity to reach the cold side of the device, and then condenses and circulates back to the heated side through capillary action. Parasitic conduction occurs through the device sidewalls. (b) Steady-state thermal resistance network for the temperature drop across the device. The resistance R_{NCG} varies with P_{NCG} and total heat input, creating the device thermal regulatory properties.

microscale gas-gap switches (primarily for cryogenic applications [24]) or liquid–vapor phase change in the form of gas-loaded heat pipes [25] and highly nonlinear boiling heat transfer coefficients [26]. With all of these different existing regulation mechanisms, however, a challenge still remains in creating versatile regulators that can be easily tuned for a wide range of operating scenarios.

In this work, we present a thermal regulator that relies on binary vapor transport through a noncondensable gas (NCG) cavity to achieve a passively switchable resistance in response to varying levels of heat input. The device resistance behavior is tunable through variation in the NCG pressure, a distinct advantage over existing regulators that are often limited to fixed switching regimes. Our previous work demonstrated a steady-state resistance OFF/ON ratio of up to 4 through this regulation mechanism, as well as an ability of the device to clamp the hot- and cold-side temperature difference to a relatively constant, heat flow independent value [27]. Here, we expand significantly upon our previous work by creating a physics-based model to explore the limits of thermal regulation based on the process of binary vapor diffusion through an NCG cavity. We present a roadmap to increase the steady-state resistance OFF/ON ratio utilizing this phenomenon to greater than 14 and define a switching efficiency metric to assess the effectiveness of the device design.

We also provide a detailed investigation of the transient thermal characteristics of the binary diffusion-based regulator, an important aspect often neglected in previous studies of thermal regulatory devices. While steady-state studies provide a baseline for relative comparison of different regulators through conventional metrics such as the switching ratio, it becomes impractical to assess their impact on system-level implementations without a thorough discussion of transient behavior. For instance, a fast response time thermal switch would be ideal for generating transient heat loads of various waveforms, such as for a pulsed energy harvester. A thermal regulator to limit sudden temperature spikes in power electronics applications, however, may benefit from additional thermal capacitance to smooth out the temperature rise. We therefore analyze the primary components that affect the thermal response time for the binary diffusion-based regulator and evaluate the switching behavior in response to a pulsed heating input. Finally, we assess the potential value of implementing this type of device in future thermal energy regulation systems and provide recommendations for possible use cases.

II. Steady-State Thermal Model

Fig. 1(a) shows a cross-sectional schematic that highlights the main working principles of the regulator. The device is comprised of a sealed chamber lined with a porous micropillar wick and charged with a fixed amount of working fluid (water) and NCG (air). Heat applied to the evaporator side of the device causes fluid in the porous wick to evaporate and then diffuse through the NCG to the condenser side, where it condenses into liquid. Capillary action then drives the condensed liquid back to the evaporator side, and the cycle repeats.

The resistance network shown in Fig. 1(b) approximates the steady-state heat transfer across the device. Heat supplied to evaporator side travels in two parallel pathways, with one portion, Q_{act}, going through the device active phase change region [outlined in red in Fig. 1(a) and (b)], and the other portion, Q_{side}, going through the device sidewalls. The parallel sidewall conduction resistance R_p can be estimated through a solid conduction simulation of the device with a dry cavity, further details of which are available in our previous work [27]. The resistance stack in the device active region includes the solid substrate, R_{sub}, the evaporator/condenser wick resistances $R_{w,e}$ and $R_{w,c}$, respectively, and the NCG/vapor mixture resistance R_{NCG}. T_e and T_c represent the average temperatures of the evaporator and condenser side substrates, respectively.

Based on the resistance network shown in Fig. 1(b), a few design guidelines emerge to optimize the resistance contrast across the device. Since R_{NCG} is the only significantly variable

resistance component, any parallel or series resistance components will minimize the overall resistance contrast. R_p should ideally be much larger than R_{NCG}; otherwise, parasitic heat flow outside of the active region leads to an undesirable thermal shunting effect that shorts the regulator. Any series resistances should ideally be as low as possible to avoid inflating the ON-state resistance and decreasing the switching contrast. The following will present physics-based models to predict the approximate values of the various parallel and series resistance components.

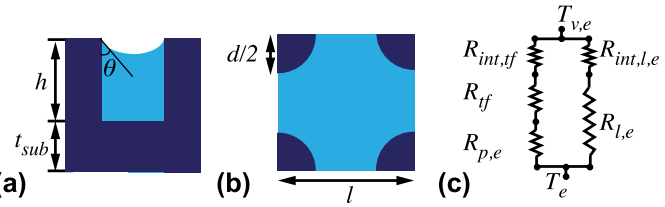

Fig. 2. (a) Micropillar wick unit cell cross-sectional view. (b) Top view of micropillar wick with diameter d and pitch l. (c) Evaporator micropillar wick resistance network.

A. Vapor Transport Model

We estimate the temperature drop across the vapor/NCG mixture by considering the vapor mass diffusion problem between the evaporator and condenser wick interfaces. The introduction of NCG presents a significant diffusion barrier to vapor transport between the evaporator and condenser. Here, we leverage the NCG to achieve a switchable device resistance due to the decrease in effective NCG resistance R_{NCG} with increased operating temperatures and heat fluxes. In the following model, we assume that the NCG and vapor exist as a binary mixture. The local component partial pressures may, therefore, be written in terms of the total chamber pressure as

$$P_{\text{tot}} = P_{\text{NCG}} + P_v. \tag{1}$$

We assume that the vapor directly above the evaporator/condenser porous wick interfaces is saturated [28], and the interface temperatures ($T_{v,e}$ and $T_{v,c}$) can be related to the vapor partial pressures ($P_{v,e}$, $P_{v,c}$) through the Clausius–Clapeyron equation. In steady state, all the liquid being evaporated must be condensed. We neglect condensation along the cavity sidewalls due to the much smaller surface area and lower external heat transfer coefficient compared with the active condenser region. Therefore, the vapor transport is 1-D and

$$\frac{d\dot{m}_v}{dz} = 0 \tag{2}$$

where $\dot{m}_v$ represents the total vapor mass flux, and the z coordinate represents the vapor flow direction between the evaporator and condenser. Heating and cooling at the evaporator/condenser surfaces set up a temperature gradient across the mixture space, resulting in a corresponding vapor mass fraction gradient. This mass fraction gradient then drives the vapor transport through the NCG barrier. Assuming insignificant dissolution of NCG at the porous wick interfaces creates a no-penetration boundary condition, where the NCG must be stationary and $\dot{m}_{\text{NCG}} = 0$. The vapor mass fraction gradient, however, creates a complementary NCG mass fraction gradient and diffusional mass flux, leading to a Maxwell–Stefan flow scenario [29]. In order to meet the zero net NCG mass flux condition, an induced counterdiffusion velocity accounting for bulk flow of the mixture counteracts the diffusional NCG flux. In steady state, this leads to the following vapor mass flux equation:

$$\dot{m}_v = \omega_v \dot{m}_{\text{tot}} - \rho_m D_{vg} \frac{d\omega_v}{dz} \tag{3}$$

where ω_v is the vapor mass fraction, ρ_m is the mixture density, and D_{vg} is the temperature-dependent, binary diffusion coefficient calculated based on the Chapman–Enskog theory [29]. From an energy balance in the device active region

$$Q_{\text{act}} = \dot{m}_v h_{fg} A \tag{4}$$

where h_{fg} is the working fluid latent heat of vaporization and A is the cross-sectional area normal to the vapor transport. Substituting (4) into (3) and integrating with respect to z links the active region heat transfer with the vapor transport equation, giving

$$Q_{\text{act}} = \frac{\rho_m D_{vg} h_{fg} A}{t_{\text{core}}} \ln\left(\frac{\omega_{v,c} - 1}{\omega_{v,e} - 1}\right) \tag{5}$$

where $\omega_{v,c}$ and $\omega_{v,e}$ are the vapor mass fractions at the condenser and evaporator sides, respectively, and t_{core} is the transport distance or cavity height.

B. Wick Resistance Model

Fig. 2(a) shows a cross-sectional schematic of a micropillar wick unit cell with height h, diameter d, and pitch l, along with the underlying substrate. The substrate thermal resistance can be calculated through a 1-D conduction resistance. The evaporator micropillar wick resistance is evaluated by considering the heat transfer pathways through the solid pillar and liquid bulk separately.

With the exception of cases involving high thermal conductivity fluids such as liquid metals, the conduction resistance of the solid pillar $R_{p,e}$ is typically much less than the conduction resistance through the liquid bulk $R_{l,e}$, and the majority of the heat traveling through the wick evaporates from a thin liquid film near the meniscus three-phase contact line. We estimate this thin-film resistance by calculating the area of an approximately 5-μm-thick liquid film around the micropillar surface for a given contact angle of θ through a force balance model in COMSOL, details of which can be found in [30] and the Supplementary Material. The thin-film conduction resistance R_{tf} is calculated by integrating the thin-film profile, treating each infinitesimal slice of liquid as a parallel resistor [31]. As the applied heat flux increases, the meniscus recedes within the micropillar wick, increasing the thin-film area and reducing the overall resistance. This effect is significant in vapor chambers and heat pipes where the evaporator resistance normally dominates the overall system resistance [32] but is expected to be minimal when the NCG resistance dominates. Therefore, we neglect any variation in

the thin-film area with applied heat flux and use a fixed contact angle θ to calculate the evaporator wick resistance. Finally, the liquid–vapor interfacial resistances in the thin-film and bulk liquid regions are calculated with the Schrage equation as

$$R_{\text{int}} = \frac{1}{A_{\text{int}}} \frac{2-\alpha}{2\alpha} \left(\frac{T_v \nu_{fg}}{h_{fg}^2} \right) \sqrt{\frac{2\pi R_u T_v}{M}} \left(1 - \frac{P_v \nu_{fg}}{2h_{fg}} \right)^{-1} \tag{6}$$

where A_{int} is the area of the interface, α is the accommodation coefficient, T_v is the vapor temperature, ν_{fg} is the vapor–liquid specific volume difference, M is the molar mass of the working fluid, and R_u is the universal gas constant [33]. Fig. 2(c) shows the overall resistance network for the evaporator wick.

The treatment of the condenser wick resistance is relatively simpler than the evaporator wick, as condensation is expected over the micropillar top surfaces as well as the liquid bulk. We therefore assume parallel heat conduction through the micropillar wick and liquid bulk with an effective thermal conductivity

$$k_{w,c} = \phi k_{\text{liq}} + (1-\phi) k_{\text{sub}} \tag{7}$$

where ϕ is the volume fraction of the wick. The final system of equations for the overall device resistance network is solved iteratively with the Trust Region Dogleg method in MATLAB to find the temperatures at each resistance node. The total device resistance is defined as

$$R_{\text{th}} = \frac{T_e - T_c}{Q} \tag{8}$$

where Q is the total heat input and equal to the sum of Q_{act} and Q_{side}. Temperature-dependent thermophysical properties of the working fluid are calculated based on tabulated values in the literature [29]. Temperature-dependent mixture properties, such as the mixture density, binary diffusion coefficient, and total chamber pressure, are evaluated using a mean temperature T_m that represents the average of the evaporator and condenser side vapor temperatures, where

$$T_m = \frac{1}{2}(T_{v,e} + T_{v,c}). \tag{9}$$

III. Experimental Procedure and Device Fabrication

The evaporator/condenser device substrates are fabricated from two 20 × 20 mm^2, 500-μm-thick pieces of silicon. The device's active area is 10 × 10 mm^2, and the extra silicon area is used for electrical contact pads and device bonding. An approximately 400-nm-thick layer of thermal oxide is grown on top of each silicon piece to provide electrical insulation for evaporated platinum serpentine thin-film resistors that simultaneously serve as heaters and resistance temperature detectors (RTDs) over the active device region. The thin-film resistors are calibrated for simultaneous use as RTDs by submerging the entire set up in a liquid bath and then creating resistance versus temperature curves with reference T-type thermocouples calibrated to an accuracy of ±0.1 °C. The porous micropillar wick structures are formed over the active device area in the evaporator/condenser substrates using ultraviolet (UV) laser ablation. A through-hole etched into the evaporator substrate facilitates liquid/NCG charging from external fluidic lines. The silicon substrates are bonded to an intermediary Pyrex insert with width w_{side} and thickness t_{core} using a glass frit seal (Koartan 5645-Si sealing glass paste) to form the device cavity. Pyrex is chosen for its matched coefficient of thermal expansion with silicon and low thermal conductivity (1 Wm^{-1}K^{-1}) to minimize the parallel conduction resistance. An approximately 1-mm-wide epoxy bead is added to the periphery of the Pyrex insert for additional mechanical stability to support the overhanging silicon areas that are not in contact with the Pyrex. Finally, a Nanoport is mounted to the etched through-hole in the evaporator side of the device with an o-ring face seal and held in place with epoxy. The maximum temperature in the experiments is limited to approximately 95 °C to prevent degradation of the sealing epoxy. Table I summarizes the overall dimensions of the various components of the device.

TABLE I
SUMMARY OF APPROXIMATE DEVICE DIMENSIONS

Parameter	w_{act} [mm]	w_{side} [mm]	t_{core} [μm]	t_{sub} [μm]	h [μm]	d [μm]	l [μm]
Value	10	1.8	500	400	100	100	200

Prior to each experiment, the device is charged with approximately 14 μL of deionized, ultrafiltered water. A copper cold plate connected to a chiller maintained at a bath temperature of 20 °C is mounted to the condenser side of the device. The device is then evacuated until the total chamber pressure reading from a pressure transducer is approximately equal to the saturation pressure of water at 20 °C, or 2.3 kPa. Ambient air is then reinjected slowly into the device until the desired total chamber pressure set point is reached. The total pressure reading P_{tot} is used in the model to calculate the starting NCG pressure P_{NCG}, assuming that the partial pressure of the vapor is equal to the saturation pressure at 20 °C. During experiments, the input power Q_{in} is supplied to the evaporator side thin-film resistor with a dc power supply. The reported steady-state power and values used in the modeling, Q, represent the input power adjusted for approximately 6% heat loss. Further details on the heat loss calculation and experimental components can be found in [27].

IV. Steady-State Model Results

A. Steady-State Model Validation

The steady-state model results for the device thermal resistance R_{th} as a function of input power are plotted with the experimental results for different levels of P_{NCG} in Fig. 3(a). Due to the maximum temperature limitation of the charging port sealing epoxy, the maximum heat input for $P_{\text{NCG}} = 99$ kPa is limited to 9 W. The model shows reasonable agreement with the experimental results and captures the decrease in R_{th} with increasing power, as well as the shift in R_{th} with varying P_{NCG}. Increasing P_{NCG} raises the vapor mass transport resistance and increases R_{th} for a given heat input. Fig. 3(b) shows the plots of the device ΔT clamping behavior for the range of P_{NCG} considered, where the temperature difference across the hot

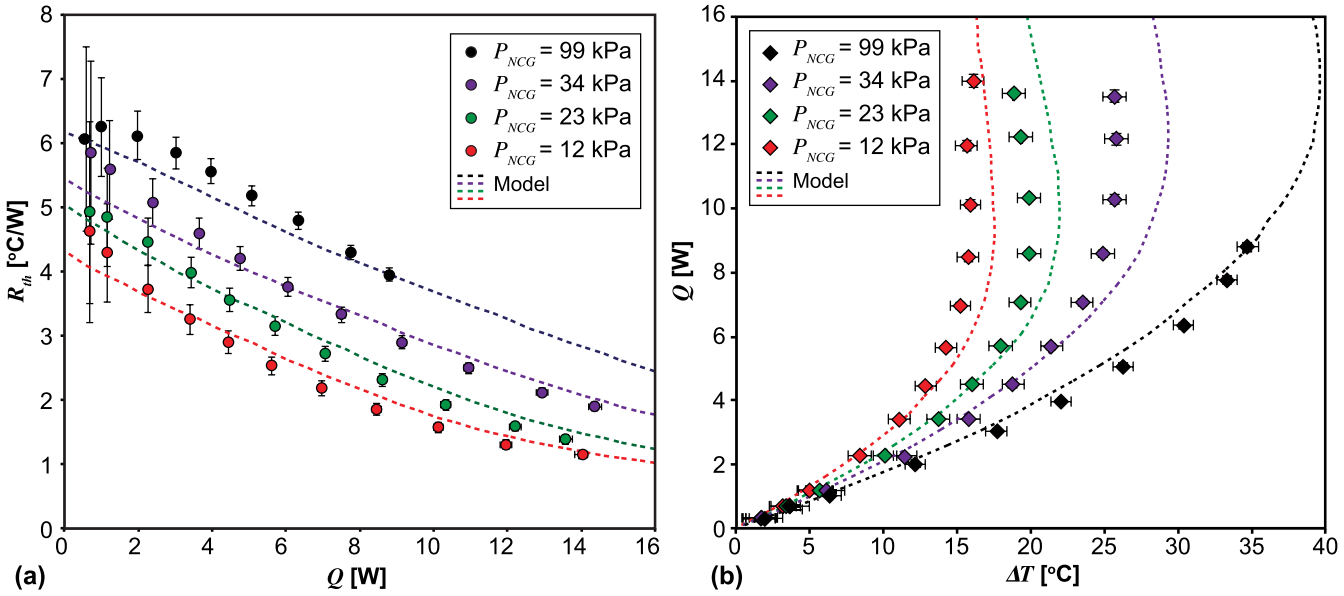

Fig. 3. (a) Steady-state experimental results for overall device resistance R_{th} for P_{NCG} = 12–99 kPa. Model prediction is shown with dashed lines. (b) Experimental results and model prediction for power Q versus temperature difference ΔT. For each P_{NCG} considered, the device clamps to a unique ΔT value and becomes relatively independent of Q. Data for P_{NCG} = 12–34 kPa are from [27].

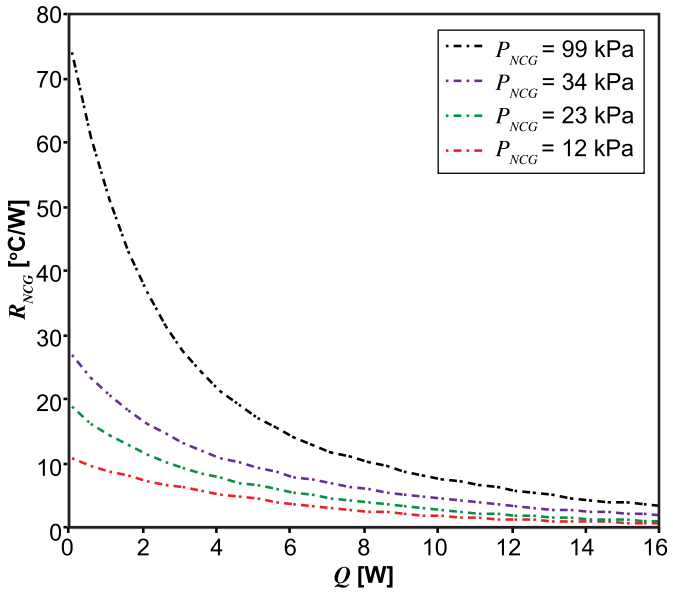

Fig. 4. Model predictions for R_{NCG} as a function of heat input for P_{NCG} = 12–99 kPa. The achievable resistance contrast in R_{NCG} is much greater than what manifests in the total device resistance R_{th} due to parallel and series resistance components.

and cold sides becomes relatively independent of Q beyond a certain threshold. As discussed in our previous work, this effect results when the hot side vapor pressure approaches the total chamber pressure P_{tot}, or $T_{v,e}$ approaches $T_{\text{sat}}(P_{\text{tot}})$ [27]. The critical clamped ΔT increases with P_{NCG}, as the required vapor pressure to initiate clamping increases correspondingly.

Fig. 4 shows the model prediction for R_{NCG} versus Q with varying P_{NCG}. For Q less than 1 W, increasing P_{NCG} from 12 to 99 kPa causes an approximately 7× increase in R_{NCG}. As shown in Fig. 3(a), however, the total device resistance R_{th} only increases by approximately 1.5×. A similar trend is observed when P_{NCG} is fixed, and the device resistance changes passively in response to varying levels of heat input. Based on Fig. 4, R_{NCG} varies by at least 10× for each P_{NCG} over the heat input range considered. R_{th}, as shown in Fig. 3(a), however, has a maximum variation of only 4× for P_{NCG} = 12 kPa. In the physical device embodiment, much of the achievable resistance contrast in R_{NCG} appears truncated due to the parallel and series resistances that decrease the overall switching effect. The following sections will therefore explore a parametric geometric optimization to increase the switching ratio through reduction of parallel heat flow pathways and series resistance components.

B. Parametric Geometric Study

The overall device resistance R_{th} can switch through two different mechanisms: active switching by varying P_{NCG} at a fixed heat input, or passive switching in response to varying levels of heat input. For the following discussion of thermal resistance switching ratio optimization, we consider the latter case and treat variation of P_{NCG} as a method of tuning the absolute device resistance and switching ratio prior to operation. This preserves the passive nature of the device, foregoes the need for additional system components to actively vary P_{NCG}, and presents a more intuitive framework to analyze the device behavior in situations such as a thermal regulator to dampen sudden power spikes. We therefore define the device switching ratio S_R as

$$S_R = \frac{R_{\text{OFF}}}{R_{\text{ON}}} = \frac{R_{\text{th}}(Q_1)}{R_{\text{th}}(Q_2)} \tag{10}$$

where Q_1 and Q_2 represent OFF-state and ON-state power inputs. For consistency with the previously reported experimental results, we consider the minimum and maximum power

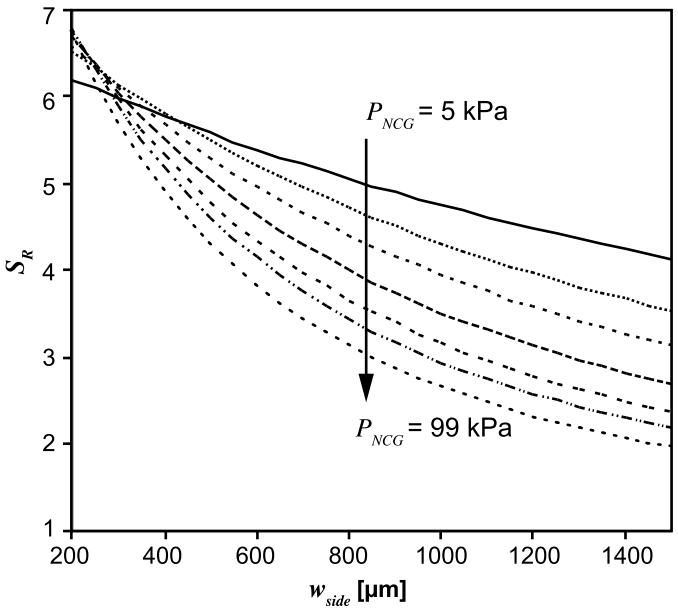

Fig. 5. Device switching ratio S_R for $t_{\text{core}} = 500\ \mu$m as the sidewall width w_{side} is varied from 200 to 1500 μm for $P_{\text{NCG}} = 5$–99 kPa. S_R is more sensitive to variations in w_{side} for higher P_{NCG}.

inputs of 0.6 and 14 W as the OFF-/ON-state powers, respectively. Note that different absolute values of switching ratios would result if different heat flow ranges were considered, though the general optimization strategies would remain the same.

1) Effect of Parallel Sidewall Conduction: We explore the effect of increasing the parallel sidewall conduction resistance R_p by varying the core thickness t_{core} and the insert width w_{side}. We simplify the calculation by neglecting any conduction through the epoxy bead, as the current purpose is merely to provide mechanical support for the extra overhanging silicon areas used for electrical contact. The modified sidewall conduction resistance is calculated as

$$R_p = \frac{t_{\text{core}}}{k_p(4w_{\text{side}}^2 + 4w_{\text{side}}w_{\text{act}})}. \tag{11}$$

Fig. 5 shows the predicted steady-state switching ratio S_R for $t_{\text{core}} = 500\ \mu$m, $w_{\text{side}} = 200$–$1500\ \mu$m, and $P_{\text{NCG}} = 5$, 11, 18, 32, 50, 67, and 99 kPa. The minimum value of w_{side} is limited to 200 μm to allow for a reasonable bonding area between the Pyrex insert and silicon substrates. Overall, reducing w_{side} leads to a higher switching ratio for all P_{NCG} considered. For w_{side} greater than approximately 500 μm, the lowest charge pressure of $P_{\text{NCG}} = 5$ kPa exhibits the highest switching ratio. A crossover regime occurs for $w_{\text{side}} < 500\ \mu$m, however, where S_R increases slightly with increasing P_{NCG}. Overall, S_R is more sensitive to variations in w_{side} as P_{NCG} is increased. A higher NCG charge pressure leads to a higher NCG resistance, which causes S_R to be more significantly limited by the parallel resistance R_p if R_p is comparable to R_{NCG} in the OFF-state. The highest NCG charge pressure considered of $P_{\text{NCG}} = 99$ kPa shows a significant increase in S_R from approximately 2 to 6.8 as w_{side} is decreased from 1500 to 200 μm.

Fig. 6(a) shows S_R as a function of P_{NCG} for $w_{\text{side}} = 200$–$1000\ \mu$m as t_{core} is increased from 500 to 1000 μm. Doubling t_{core} for the range of parameters considered successfully increases S_R to greater than 10. As w_{side} decreases, S_R becomes less dependent on P_{NCG}. As shown in Fig. 6(a), S_R is fairly constant for $w_{\text{side}} = 200\ \mu$m and varies by less than ± 0.2 for all P_{NCG} considered. When $R_p \gg R_{\text{NCG}}$, R_{NCG} governs the overall device resistance. Increasing P_{NCG}, therefore, causes both the OFF-state and ON-state resistances to shift fairly proportionally, and the total switching ratio is less sensitive to P_{NCG}. When $R_p \sim R_{\text{NCG}}$, however, R_p limits the OFF-state resistance, and increasing P_{NCG} serves to increase the overall ON-state resistance only, reducing S_R.

We further explore this phenomena by defining a switching efficiency for the device, η, equal to the overall device OFF-/ON-resistance ratio divided by the NCG OFF-/ON-resistance ratio

$$\eta = \frac{R_{\text{th}}(Q_1)/R_{\text{th}}(Q_2)}{R_{\text{NCG}}(Q_1)/R_{\text{NCG}}(Q_2)} = \frac{S_R}{S_{\text{NCG}}} \tag{12}$$

where S_{NCG} is the switching ratio of R_{NCG} at the OFF-/ON-state heat inputs. A value of η approaching 1, therefore, means that the device is approaching the limits of the maximum possible switching ratio for a given P_{NCG}. Fig. 6(b) shows the calculated switching efficiencies over the range of P_{NCG} considered for $t_{\text{core}} = 1000\ \mu$m and $w_{\text{side}} = 200$–$1000\ \mu$m. For the current configuration considered, the efficiency peaks at 0.66 for P_{NCG} approximately equal to 30 kPa and $w_{\text{side}} = 200\ \mu$m.

2) Effect of Porous Wick Thermal Resistance: In addition to the parallel resistance of R_p, resistance components in series with R_{NCG} also play an important role in limiting the overall device switching efficiency. In the OFF-state, R_{NCG} is large and dominates the overall series resistance stack. As Q increases, however, R_{NCG} decreases steadily and becomes comparable to the next largest series resistance component, which is the evaporator micropillar wick resistance $R_{w,e}$. The ON-state resistance thus potentially becomes governed by $R_{w,e}$, further limiting the switching contrast. A more detailed discussion of the relative contribution of each component to the total stack resistance is included in the Supplementary Material.

To investigate the effect of varying the micropillar wick resistance, the micropillar dimensions were modified from the values listed in Table I to include cases with diameters $d = 12$, 25, and 50 μm and pitches $l = 25$, 50, and 100 μm. Moving to a finer wick creates more evaporative heat transfer surface area and reduces the overall wick resistance. A denser wick also creates a higher viscous flow resistance, however, potentially limiting the capillary-driven maximum heat flux of the device. A fluid flow simulation was performed for each micropillar array dimension in COMSOL to confirm that the maximum heat input considered in each case could be sustained without capillary-limited dryout (details in the Supplementary Material). In each case, the total viscous pressure drop across the wick for an ON-state heat input of 14 W was less than 13% of the estimated capillary pressure, well below the dryout limit.

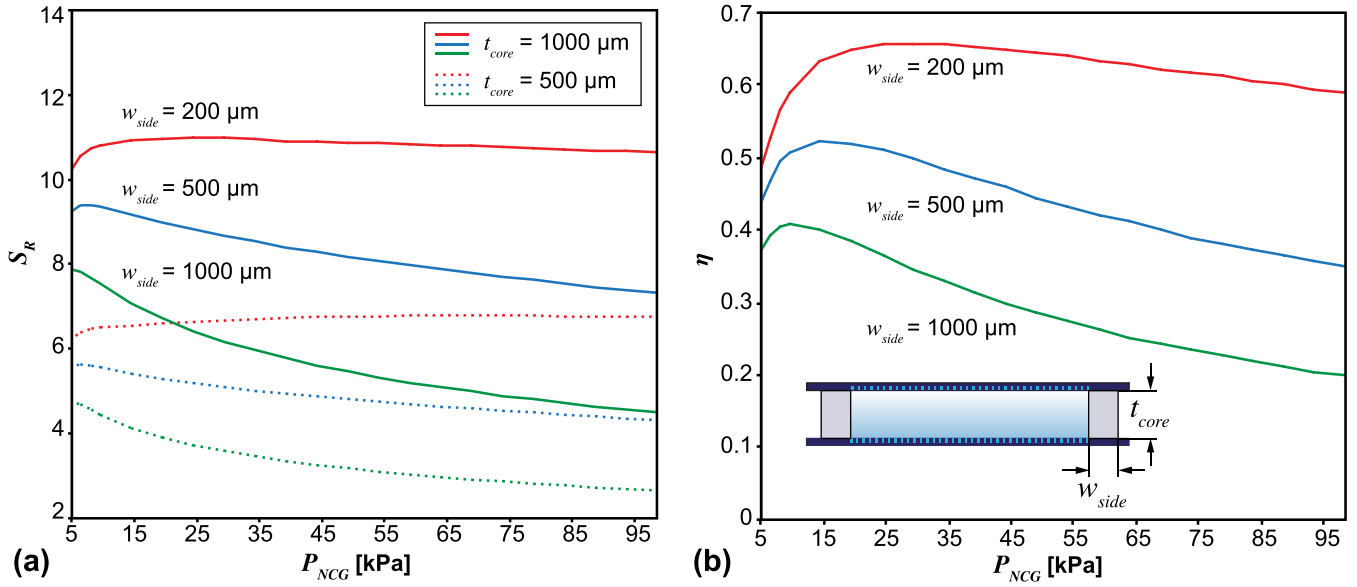

Fig. 6. (a) Device switching ratio S_R for sidewall width w_{side} = 200–1000 μm, P_{NCG} = 5–99 kPa, and t_{core} = 500–1000 μm. Increasing t_{core} is more effective for increasing S_R as w_{side} is reduced to prevent R_p and R_{NCG} from scaling proportionately. (b) Switching efficiency of the device, η, for t_{core} = 1000 μm and w_{side} = 200–1000 μm.

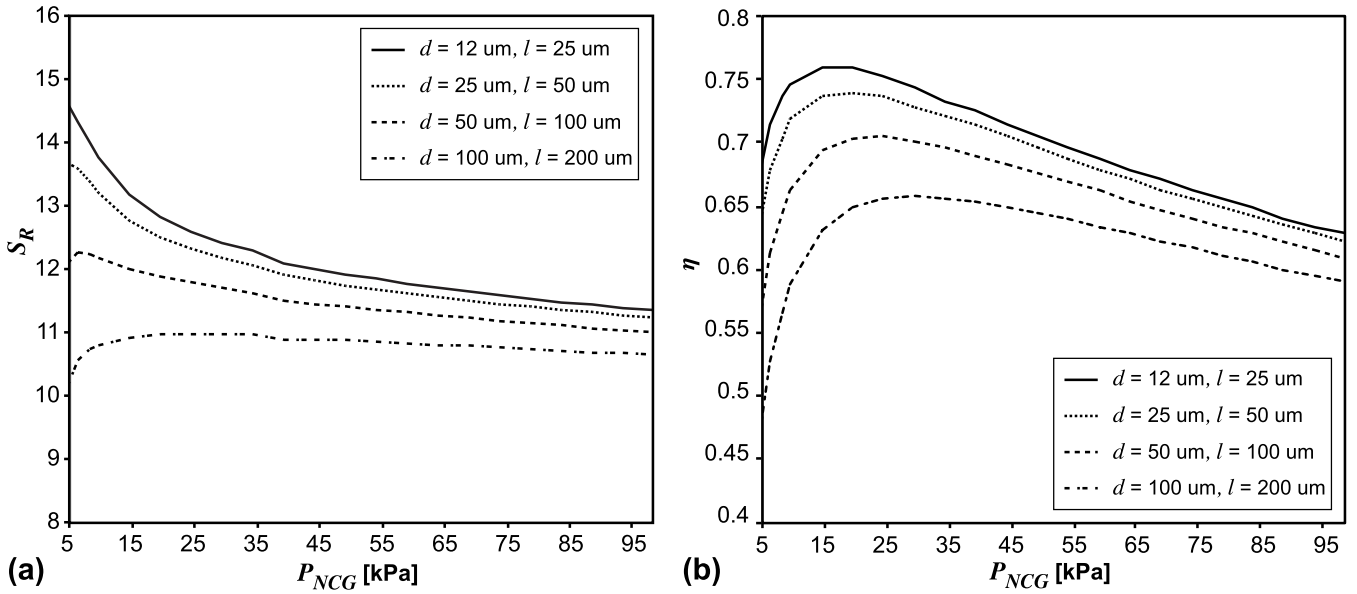

Fig. 7. (a) Switching ratio S_R as a function of P_{NCG} for w_{side} = 200 μm and t_{core} = 1000 μm as micropillar wick dimensions are varied from d = 12 to 100 μm and l = 25 to 200 μm. Reducing $R_{w,e}$ with a higher density pillar array has the most significant impact on increasing S_R in the low P_{NCG} range. (b) Switching efficiency η with varied micropillar array dimensions to reduce $R_{w,e}$. A maximum efficiency of approximately 0.76 is reached for the finest pillar dimensions considered of d = 12 μm and l = 25 μm.

Fig. 7(a) shows the variation in S_R as a function of P_{NCG} for the different micropillar dimensions considered with w_{side} = 200 μm and t_{core} = 1000 μm. Reducing the overall wick resistance appears to have the most significant impact on S_R in the low P_{NCG} range. A maximum switching ratio of approximately 14.5 is achieved for the highest density wick with P_{NCG} = 5 kPa. For higher P_{NCG}, R_{NCG} remains substantially higher than $R_{w,e}$ in the ON-state and continues to dominate the resistance stack, minimizing the impact of reducing $R_{w,e}$. This is also evidenced in Fig. 7(b) that shows the plots of the switching efficiency η for each of the different micropillar array dimensions considered. As the overall wick resistance is decreased, the maximum efficiency point shifts left toward lower values of P_{NCG}, with a maximum η reached of approximately 0.76 for the finest micropillar wick dimensions considered of d = 12 μm and l = 25 μm. Lower P_{NCG} levels, therefore, appear sufficient to create a high switching ratio thermal regulator, but higher P_{NCG} levels can be used to tune the absolute OFF-/ON-state resistances.

V. Transient Device Characteristics

Based on the results in Section IV, the steady-state switching ratio can be significantly enhanced by tuning various aspects of the device geometry. While this demonstrates a clear path for optimizing future design iterations, considering the steady-state resistance only provides an incomplete picture of how the device would function in practice, as thermal regulation by nature is needed as a response mechanism for managing/creating transient thermal events.

A. Transient Thermal Model

For the transient thermal analysis, we assume that the timescale associated with the vapor diffusion is much smaller than the thermal response time of the device solid portions [34], [35]. Similarly, we neglect the effect of varying liquid velocities in the porous wick and assume that the steady-state conduction model remains sufficient to describe the heat transfer across the micropillar arrays [36], [37]. With this treatment, the majority of the transient device behavior is governed by sensible heat storage. The resistance of the NCG/vapor core is comparable to the condenser side external heat transfer resistance, meaning that the transient device behavior cannot be accurately modeled with a lumped analysis as done for heat pipes [38]. Therefore, we use a 3-D solid conduction model in COMSOL to capture the device transient behavior. The NCG/vapor core mixture is modeled as a block with an NCG pressure- and temperature-dependent effective thermal conductivity derived from the steady-state model results. Due to the small mass of NCG/vapor contained in the core, the thermal capacitance of the mixture is expected to be negligible compared with the wick and solid portions of the device (on the order of 1e-5 J/K). The evaporator/condenser effective wick thermal conductivities are similarly calculated using the steady-state model, with equivalent densities and heat capacities calculated based on the wick porosity, ϕ, as

$$\rho_w = \phi\rho_{\text{liq}} + (1-\phi)\rho_{\text{sub}} \tag{13}$$

$$c_{p,w} = \phi c_{p,\text{liq}} + (1-\phi)c_{p,\text{sub}} \tag{14}$$

where ρ and c_p represent the different densities and heat capacities of various components, respectively. A full list of the properties used for the various device components and further simulation details can be found in the Supplementary Material. We note that if significant redistribution of liquid occurs within the device such as liquid starvation within the wick, it may no longer be accurate to model the wicks and NCG/vapor mixture as blocks with equivalent thermal conductivities and heat capacities. The model is, therefore, only appropriate for heat input ranges within the capillary limits of the device operation.

B. Transient Experimental Validation and Results

Fig. 8 shows the transient model and experimental device temperature profiles as the power to the heater is first stepped up to approximately 9 W and then stepped down to 0.7 W for $P_{\text{NCG}} = 12$ kPa and $t_{\text{core}} = 500$ μm. Overall, the model shows fair agreement with the experimental temperature profiles,

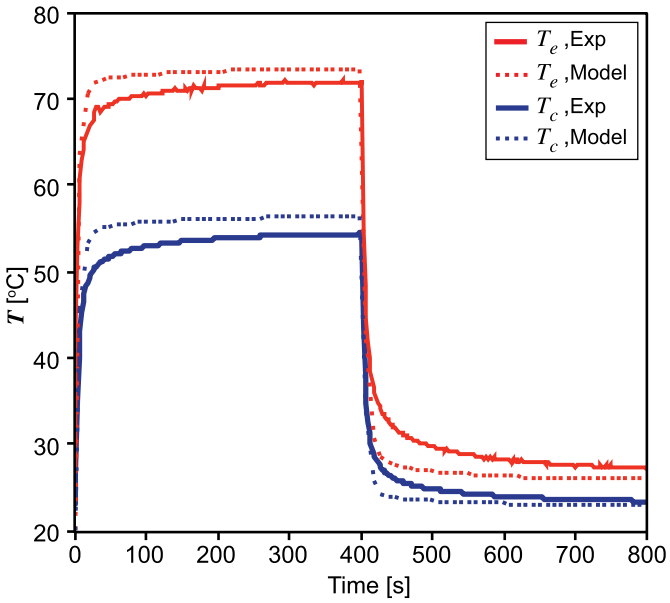

Fig. 8. Transient model and experimental temperature profiles for the average evaporator/condenser side temperatures T_e and T_c in response to step high- and low-heat inputs of approximately 9 and 0.7 W, respectively.

TABLE II

Thermal Time Constant τ_h as a Function of External Condenser Side Heat Transfer Coefficient h_{CP}

h_{cp}[Wm^{-2}K^{-1}]	τ_h[s]
500	15.3
2400	4.4
5000	1.8
10,000	1

confirming the assumption that the majority of the transient temperature response is governed by sensible heat storage. We assess the device thermal response time in terms of a time constant τ_h, which represents the time required for T_e to reach 63% of the total steady-state temperature rise. The model and experimental values for τ_h agree well with values of approximately 4.4 and 4.9 s, respectively. In addition to the internal device resistances, τ_h also depends strongly on the external condenser side heat transfer coefficient h_{cp}. As h_{cp} is varied from 500 to 10 000 Wm^{-2}K^{-1}, τ_h ranges from approximately 15 to 1 s. The model results for τ_h as a function of h_{cp} are listed in Table II. h_{cp} is approximately equal to 2400 Wm^{-2}K^{-1} in the experiments.

Fig. 9(a) shows the transient temperature profiles in response to a pulsed heating input, where Q_{in} is modulated between ON-/OFF-state powers of 9 and 0.7 W, respectively, over a period of 10 s for $P_{\text{NCG}} = 12$ kPa and $t_{\text{core}} = 500$ μm. As shown in the plot, the applied heat input is not a true square wave due to the temperature-dependent resistance of the serpentine heater/RTD. To account for this, the experimentally measured heating profile is directly used as a simulation input. Fig. 9(b) shows the effective device resistance in response to the pulsed heat input. As shown in Fig. 9(b), the device responds rapidly when transitioning from the OFF-state to ON-state and reaches the steady-state ON-state resistance with

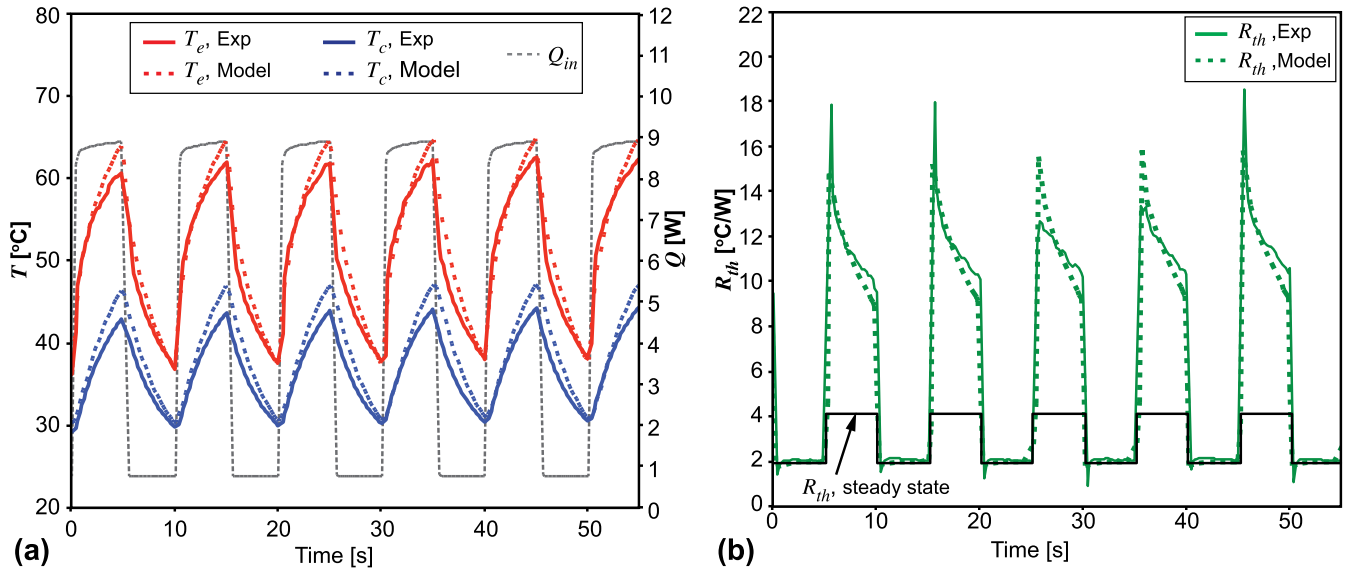

Fig. 9. (a) Model and experimental temperature profiles when the applied heat input Q_{in} is pulsed in 5-s durations from 0.7 to 9 W. (b) Transient device resistance in response to the pulsed heating input. The device takes longer to reach the steady-state resistance value in the cool-down phase, leading to transient OFF-state resistances much higher than steady-state values.

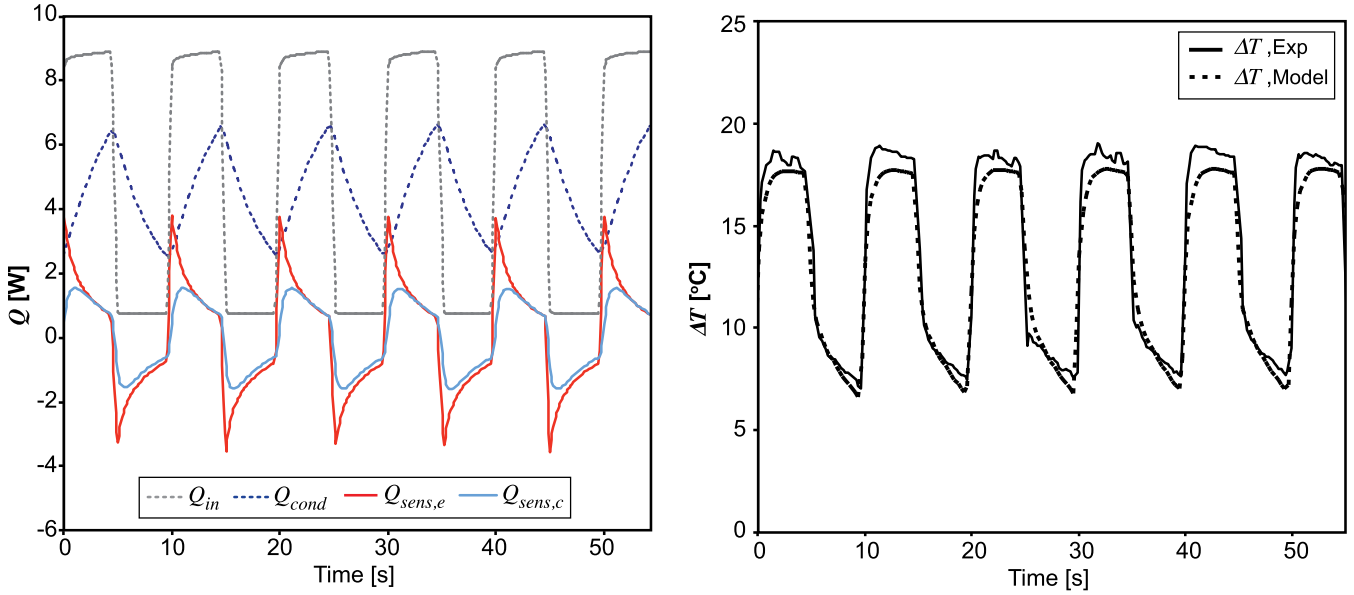

Fig. 10. (a) Model results for the device transient heat flow pathways in terms of the total heat supplied to the heater, external heat removal from the condenser side, and the rate of change in sensible heat storage in the evaporator/condenser substrates. (b) Transient model and experimental profiles for the temperature difference ΔT in response to a pulsed heat input. The clamping behavior of the device fixes ΔT in the ON-state and causes the device resistance to rapidly approach the steady-state value.

almost no delay. When the heat load is reduced, however, the difference in the response times of the condenser and evaporator sides leads to a large spike in the apparent device OFF-state resistance up to as high as 18 °C/W. This is much higher than the predicted steady-state resistance value of approximately 4 °C/W. The OFF-state resistance slowly declines over 5 s to around 8 °C/W but still remains approximately 2× greater than the steady-state value. This leads to an interesting phenomenon, where the transient switching ratio appears significantly higher than the steady-state ratio. We note that the use of the steady-state thermal resistance and switching ratio definitions for a transient heating scenario is limited. Unlike the steady-state definition, the transient resistance does not represent an inherent property of the device that governs the temperature drop for a given heat input, as the heat flow distribution within the device varies with time. However, such a definition does provide a convenient framework to highlight the asymmetry in the device behavior when switching between OFF–ON and ON–OFF transitions.

The difference between the OFF–ON and ON–OFF transitions can be explained by considering the heat transport pathways in the two different scenarios. Fig. 10(a) shows the model

results for the transient heat flow pathways within the device in terms of the heat applied to the heater, Q_{in}, the amount of heat removed from the condenser side, Q_{cond}, and the rate of change in sensible heat storage in the evaporator/condenser side substrates, $Q_{\text{sens},e}$ and $Q_{\text{sens},c}$, respectively. As heat is supplied to the evaporator side heater, a significant portion of the heat is initially stored as sensible heat in the evaporator side substrate. The heat eventually reaches the condenser side, increasing the amount of heat rejection through the external cold plate. $Q_{\text{sens},e}$ and $Q_{\text{sens},c}$ approach the same value approximately 2 s after the initial heating pulse and decline steadily as Q_{cond} continues to rise.

In the cool-down phase, Q_{in} is suddenly decreased, and an excess amount of heat is removed from the condenser side. Some amount of variation in the transient resistance response of the device for ON–OFF and OFF–ON transitions is expected, as the higher steady-state device resistance in the OFF-state naturally increases the thermal time constant for the absolute temperature response. The asymmetry of the transient resistance is primarily dominated, however, by the ΔT clamping behavior of the device, as shown in Fig. 10(b). In the ON-state, enough heat is supplied that the device crosses the ΔT clamping threshold [as shown in Fig. 3(b)], and the temperature difference across the device becomes relatively independent of heat flow. This causes ΔT to quickly approach a fixed value of approximately 18 °C with relatively minimal impact from sensible heat storage within the device. In the OFF-state, the device falls outside of the ΔT clamping regime as the heat input is reduced, and the ΔT heat flow dependence returns. The effect of sensible heat storage becomes more apparent, and ΔT decreases with time to approach the steady-state value. The high apparent transient OFF-state resistance is, therefore, not a true change in device resistance but an effect of sensible heat storage that causes ΔT to be higher than the steady-state value. The combination of this with the ability of the device to clamp to a fixed ΔT above a certain threshold leads to the asymmetric transient behavior, where the OFF–ON resistance response time appears much shorter than the ON–OFF resistance response time. The transient switching ratio of the device therefore also appears higher than the steady-state ratio due to the combined effect of sensible heat storage in the OFF-state and temperature clamping in the ON-state.

VI. Conclusion

The results from the steady-state switching ratio optimization demonstrate that binary vapor diffusion through an NCG cavity is an effective mechanism for creating a tunable, high thermal resistance contrast device. Careful consideration of the overall device design is necessary, however, to minimize parasitic conduction pathways and fully employ the maximum achievable resistance contrast with the vapor diffusion process. When parasitic conduction and series resistances are sufficiently reduced, the device can achieve a switching ratio of up to 14.5 when transitioning between OFF-/ON-state power inputs of 0.6 and 14 W. Larger switching ratios are also possible depending on the OFF-/ON-state powers under consideration. We note that the parasitic conduction pathway through the Pyrex insert can only be reduced to a certain limit before the mechanical integrity of the device suffers, however, due to both the increasing fragility of the Pyrex frame as well as the reduction in bonding area with the silicon substrates. Future work involving mechanical simulations would be valuable to add another consideration to the device performance optimization.

Transient experiments and modeling of the regulator revealed that the majority of the device's thermal capacitance is comprised of sensible heat storage in the solid device volume. The device thermal time constant ranges from approximately 1 to 15 s depending on the external heat transfer coefficient. For transient events occurring with significantly shorter time scales, the device will likely not be able to respond fast enough for resistance switching to occur. For transient events occurring on the order of a few seconds, the temperature clamping behavior of the device creates a highly attractive attribute where the ON-state resistance of the device is reached relatively quickly, and the apparent OFF-state resistance is magnified over the steady-state value. This asymmetric transient response promotes the device as a good candidate for use as a thermal regulator to mitigate sudden temperature swings. The temperature clamping behavior can also potentially create a thermal buffering effect to protect sensitive components from fluctuations in ambient environmental conditions [12]. However, larger-scale modeling is required to predict the effect of implementing the device in a system-level regulation scenario, as the overall temperature response will depend on the system-level thermal resistances and capacitances. With this work, the aim is to produce an accurate picture of the standalone regulator behavior that can feed into future system-level experiments and/or models.

Acknowledgment

Part of this work was performed at the Stanford Nano Shared Facilities (SNSF)/Stanford Nanofabrication Facility (SNF), supported by the NSF under Award ECCS-1542152. The authors thank N. Miljkovic for technical discussions and feedback. Any opinions, findings, and conclusions or recommendations expressed in this material are those of the authors and do not necessarily reflect the views of the National Science Foundation.

References

[1] A. Bhunia, S. Chandrasekaran, and C.-L. Chen, "Performance improvement of a power conversion module by liquid micro-jet impingement cooling," *IEEE Trans. Compon. Packag. Technol.*, vol. 30, no. 2, pp. 309–316, Jun. 2007.

[2] R. Pittini, S. D'Arco, M. Hernes, and A. Petterteig, "Thermal stress analysis of IGBT modules in VSCS for PMSG in large offshore wind energy conversion systems," in *Proc. 14th Eur. Conf. Power Electron. Appl.*, Aug./Sep. 2011, pp. 1–10.

[3] J. Gong, G. Cha, Y. Sungtaek Ju, and C.-J. Kim, "Thermal switches based on coplanar EWOD for satellite thermal control," in *Proc. IEEE 21st Int. Conf. Micro Electro Mech. Syst.*, Jan. 2008, pp. 848–851.

[4] D. J. Sadler, R. Changrani, P. Roberts, C.-F. Chou, and F. Zenhausern, "Thermal management of BioMEMS: Temperature control for ceramic-based PCR and DNA detection devices," *IEEE Trans. Compon. Packag. Technol.*, vol. 26, no. 2, pp. 309–316, Jun. 2003.

[5] C. T. Wittwer and D. J. Garling, "Rapid cycle dna amplification: Time and temperature optimization," *Biotechniques*, vol. 10, no. 1, pp. 76–83, 1991.

[6] B. J. Brinkworth, B. M. Cross, R. H. Marshall, and H. Yang, "Thermal regulation of photovoltaic cladding," *Sol. Energy*, vol. 61, no. 3, pp. 169–178, Sep. 1997.

[7] A. M. Elbreki, M. A. Alghoul, K. Sopian, and T. Hussein, "Towards adopting passive heat dissipation approaches for temperature regulation of PV module as a sustainable solution," *Renew. Sustain. Energy Rev.*, vol. 69, pp. 961–1017, Mar. 2017.

[8] V. Smet *et al.*, "Ageing and failure modes of IGBT modules in high-temperature power cycling," *IEEE Trans. Ind. Electron.*, vol. 58, no. 10, pp. 4931–4941, Oct. 2011.

[9] Y. Yan and J. A. Malen, "Periodic heating amplifies the efficiency of thermoelectric energy conversion," *Energy Environ. Sci.*, vol. 6, no. 4, pp. 1267–1273, 2013.

[10] I. S. McKay and E. N. Wang, "Thermal pulse energy harvesting," *Energy*, vol. 57, pp. 632–640, Aug. 2013.

[11] R. McCarty, K. P. Hallinan, B. Sanders, and T. Somphone, "Enhancing thermoelectric energy recovery via modulations of source temperature for cyclical heat loadings," *J. Heat Transf.*, vol. 129, no. 6, pp. 749–755, Jun. 2007.

[12] G. Wehmeyer, T. Yabuki, C. Monachon, J. Wu, and C. Dames, "Thermal diodes, regulators, and switches: Physical mechanisms and potential applications," *Appl. Phys. Rev.*, vol. 4, no. 4, Dec. 2017, Art. no. 041304.

[13] T. Slater, P. Van Gerwen, E. Masure, F. Preud'homme, and K. Baert, "Thermomechanical characteristics of a thermal switch," *Sens. Actuators A, Phys.*, vol. 53, nos. 1–3, pp. 423–427, May 1996.

[14] C. Y. Tso and C. Y. H. Chao, "Solid-state thermal diode with shape memory alloys," *Int. J. Heat Mass Transf.*, vol. 93, pp. 605–611, Feb. 2016.

[15] M. Hao, J. Li, S. Park, S. Moura, and C. Dames, "Efficient thermal management of li-ion batteries with a passive interfacial thermal regulator based on a shape memory alloy," *Nature Energy*, vol. 3, no. 10, pp. 899–906, Oct. 2018.

[16] M. A. dos Santos Bernardes, "Experimental evidence of the working principle of thermal diodes based on thermal stress and thermal contact conductance–thermal semiconductors," *Int. J. Heat Mass Transf.*, vol. 73, pp. 354–357, Jun. 2014.

[17] T. Yang *et al.*, "An integrated liquid metal thermal switch for active thermal management of electronics," *IEEE Trans. Compon., Packag., Manuf., Technol.*, vol. 9, no. 12, pp. 2341–2351, Dec. 2019.

[18] S.-H. Jeong, W. Nakayama, and S.-K. Lee, "Experimental investigation of a heat switch based on the precise regulation of a liquid bridge," *Appl. Thermal Eng.*, vol. 39, pp. 151–156, Jun. 2012.

[19] J. Cho, T. Wiser, C. Richards, D. Bahr, and R. Richards, "Fabrication and characterization of a thermal switch," *Sens. Actuators A, Phys.*, vol. 133, no. 1, pp. 55–63, Jan. 2007.

[20] H.-K. Lyeo *et al.*, "Thermal conductivity of phase-change material $Ge_2Sb_2Te_5$," *Appl. Phys. Lett.*, vol. 89, no. 15, 2006, Art. no. 151904.

[21] D.-W. Oh, C. Ko, S. Ramanathan, and D. G. Cahill, "Thermal conductivity and dynamic heat capacity across the metal-insulator transition in thin film VO2," *Appl. Phys. Lett.*, vol. 96, no. 15, Apr. 2010, Art. no. 151906.

[22] P. Ben-Abdallah and S.-A. Biehs, "Phase-change radiative thermal diode," *Appl. Phys. Lett.*, vol. 103, no. 19, Nov. 2013, Art. no. 191907.

[23] R. Shrestha *et al.*, "High-contrast and reversible polymer thermal regulator by structural phase transition," *Sci. Adv.*, vol. 5, no. 12, Dec. 2019, Art. no. eaax3777.

[24] I. Catarino, G. Bonfait, and L. Duband, "Neon gas-gap heat switch," *Cryogenics*, vol. 48, nos. 1–2, pp. 17–25, Jan. 2008.

[25] I. Sauciuc, A. Akbarzadeh, and P. Johnson, "Temperature control using variable conductance closed two-phase heat pipe," *Int. Commun. Heat Mass Transf.*, vol. 23, no. 3, pp. 427–433, May 1996.

[26] C. Zhang, J. W. Palko, M. T. Barako, M. Asheghi, J. G. Santiago, and K. E. Goodson, "Enhanced capillary-fed boiling in copper inverse opals via template sintering," *Adv. Funct. Mater.*, vol. 28, no. 41, Oct. 2018, Art. no. 1803689.

[27] T. Liu *et al.*, "Tunable, passive thermal regulation through liquid to vapor phase change," *Appl. Phys. Lett.*, vol. 115, no. 25, Dec. 2019, Art. no. 254102.

[28] J. Huang, J. Zhang, and L. Wang, "Review of vapor condensation heat and mass transfer in the presence of non-condensable gas," *Appl. Thermal Eng.*, vol. 89, pp. 469–484, Oct. 2015.

[29] I. J. H. Lienhard and V. J. H. Lienhard, *A Heat Transfer Textbook*. Cambridge, MA, USA: Phlogiston Press, 2006.

[30] Y. Zhu, D. S. Antao, Z. Lu, S. Somasundaram, T. Zhang, and E. N. Wang, "Prediction and characterization of dry-out heat flux in micropillar wick structures," *Langmuir*, vol. 32, no. 7, pp. 1920–1927, Feb. 2016.

[31] T. Liu, M. T. Dunham, K. W. Jung, B. Chen, M. Asheghi, and K. E. Goodson, "Characterization and thermal modeling of a miniature silicon vapor chamber for die-level heat redistribution," *Int. J. Heat Mass Transf.*, vol. 152, May 2020, Art. no. 119569.

[32] D. Ćoso, V. Srinivasan, M.-C. Lu, J.-Y. Chang, and A. Majumdar, "Enhanced heat transfer in biporous wicks in the thin liquid film evaporation and boiling regimes," *J. Heat Transf.*, vol. 134, no. 10, Oct. 2012.

[33] V. P. Carey, *Liquid Vapor Phase Change Phenomena: An Introduction to the Thermophysics of Vaporization and Condensation Processes in Heat Transfer Equipment*. Boca Raton, FL, USA: CRC Press, 2020.

[34] C. Harley and A. Faghri, "Transient two-dimensional gas-loaded heat pipe analysis," *J. Heat Transf.*, vol. 116, no. 3, pp. 716–723, Aug. 1994.

[35] B. D. Marcus, *Theory Design Variable Conductance Heat Pipes*. Washington, DC, USA: National Aeronautics and Space Administration, 1972.

[36] Y. Cao and A. Faghri, "Transient two-dimensional compressible analysis for high-temperature heat pipes with pulsed heat input," *Numer. Heat Transf., A, Appl.*, vol. 18, no. 4, pp. 483–502, Jan. 1991.

[37] Y. Wang and K. Vafai, "Transient characterization of flat plate heat pipes during startup and shutdown operations," *Int. J. Heat Mass Transf.*, vol. 43, no. 15, pp. 2641–2655, Aug. 2000.

[38] A. Faghri and C. Harley, "Transient lumped heat pipe analyses," *Heat Recovery Syst. CHP*, vol. 14, no. 4, pp. 351–363, Jul. 1994.

Tanya Liu received the B.S. degree in mechanical engineering from the Massachusetts Institute of Technology, Cambridge, MA, USA, in 2014. She is currently pursuing the Ph.D. degree in mechanical engineering with Stanford University, Stanford, CA, USA.

Her current research interests include active and passive thermal management strategies for high power electronics and liquid-to-vapor phase change phenomena in porous media.

Ms. Liu was a recipient of the National Science Foundation Graduate Research Fellowship.

James W. Palko received the B.S. degree in mechanical engineering from Arkansas Tech University, Russellville, AR, USA, and the M.S. and Ph.D. degrees in materials science and engineering from the University of Illinois at Urbana–Champaign, Champaign, IL, USA.

He was a Hertz Fellow with the University of Illinois at Urbana–Champaign. He has served on the Research Staff at Stanford University, Stanford, CA, USA, and has also worked in the aerospace and alternative energy industries. He is currently an Assistant Professor of mechanical engineering with the University of California at Merced, Merced, CA, USA. His group focuses on a range of thermal and electrokinetic transport phenomena with applications spanning from thermal management to energy storage and water purification.

Joseph S. Katz received the B.S. degree in electrical engineering from Purdue University, West Lafayette, IN, USA, in 2012, and the M.S. and Ph.D. degrees in electrical engineering from Stanford University, Stanford, CA, USA, in 2014 and 2019, respectively. His Ph.D. thesis focused on thermal conduction in soft materials.

In 2019, he joined Exponent, Menlo Park, CA, USA, as an Associate, where he works on electronic failure analysis.

Feng Zhou (Member, IEEE) received the Ph.D. degree in mechanical engineering from the University of California at Los Angeles, Los Angeles, CA, USA.

He is currently a Senior Scientist with the Electronics Research Department, Toyota Research Institute of North America, Ann Arbor, MI, USA. He has authored 15 articles in archival journals and over 20 articles in conference proceedings. He holds six issued U.S. patents and over 20 pending patents. His current research interests include advanced cooling and heat spreading solutions, micro-electromechanical system (MEMS) fabrication, vehicle-waste heat recovery, and integrated motor drive solutions.

Dr. Zhou received the R&D 100 Award for the development of next-generation power electronics for electrified vehicles.

Ercan M. Dede (Member, IEEE) received the B.S. and Ph.D. degrees in mechanical engineering from the University of Michigan, Ann Arbor, MI, USA, and the M.S. degree in mechanical engineering from Stanford University, Stanford, CA, USA.

He is currently the Group Manager of the Electronics Research Department, Toyota Research Institute of North America, Ann Arbor. His team focuses on vehicle systems involving advanced sensors, power semiconductors, electronics and photonics packaging, and thermal management technology. He has over 110 issued patents and has published more than 85 articles in archival journals and conference proceedings on topics related to design and structural optimization of thermal, mechanical, and electromagnetic systems. He is the author of the book entitled *Multiphysics Simulation: Electromechanical System Applications and Optimization*.

Dr. Dede's team received two R&D 100 Awards for the development of technologies related to next-generation electronics for electrified vehicles.

Mehdi Asheghi (Member, IEEE) received the Ph.D. degree from Stanford University, Stanford, CA, USA.

He completed his post-doctoral studies at Stanford University through research on nanoscale thermal engineering of microelectronic devices, including several highly cited articles on phonon conduction in silicon layers. He led a very well-funded research program at Carnegie Mellon University, Pittsburgh, PA, USA, from 2000 to 2006, which focused on nanoscale thermal phenomena in semiconductor and data storage devices. At Stanford University, his research ranges from nanoscale memory technologies to two-phase microfluidics. He is the author of more than 200 journal publications, fully reviewed conference papers, and book chapters.

Dr. Asheghi was the Technical Program Chair and the General Chair of the Intersociety Conference on Thermal and Thermomechanical Phenomena in Electronic Systems (ITHERM) 2012 and 2014 and the International Technical Conference and Exhibition on Packaging and Integration of Electronic and Photonic Microsystems (InterPACK) 2015 and 2017.

Kenneth E. Goodson (Fellow, IEEE) cofounded Cooligy, Mountain View, CA, USA, which built heat sinks for Apple desktops. He is currently the Davies Family Provostial Professor and a Senior Associate Engineering Dean with Stanford University, Stanford, CA, USA, where he holds appointments in mechanical engineering and (by courtesy) materials science. His 45 Ph.D. graduates are distributed evenly among IC companies and professorships at top schools, including the Massachusetts Institute of Technology (MIT), Cambridge, MA, USA, Stanford University, and the University of California at Berkeley (UC Berkeley), Berkeley, CA, USA. He holds 35 patents.

Dr. Goodson is a member of the National Academy of Engineering and a Fellow with the American Society of Mechanical Engineers (ASME), the American Physical Society (APS), the American Association for the Advancement of Science (AAAS), and the National Academy of Inventors (NAI). His awards include the ASME Kraus Medal, the Inaugural IEEE Richard Chu Award, the AIChE Kern Award, and the SRC Technical Excellence and University Researcher Awards. He recently served as the Stanford Mechanical Engineering Chair and recruited 15 faculty who transformed the department's scholarship and diversity.